Integrated Polarization Beam Splitter for 100/400 GE Polarization Multiplexed Coherent Optical Communications

Diego Pérez-Galacho, Ruiyong Zhang, Alejandro Ortega-Moñux, Robert Halir, Carlos Alonso-Ramos, Patrick Runge, Klemens Janiak, Gan Zhou, Heinz-Gunter Bach, Andreas G. Steffan, and Íñigo Molina-Fernández

***Abstract*—Monolithically integrated polarization management is a key objective for the next generation of high speed optical coherent receivers, and will enable transmission rates up to 400 Gbps. In this work we present a polarization beam splitter (PBS) based on an asymmetrical Mach–Zehnder interferometer (MZI) monolithically integrated with a coherent receiver. Thermal tuning is incorporated on the MZI arms to partially compensate fabrication errors. We propose a complete model that predicts that thermal tuning can furthermore be used to adjust the wavelength response of the PBS. Measurements on a fully integrated receiver validate this model. We show full tunability of the PBS response within the C-band, with a polarization extinction ratio in excess of 16 dB for devices with an estimated width error up to 75 nm.**

***Index Terms*—Coherent optical communications, indium phosphide, integrated optics, polarization beam splitter, polarization management.**

I. Introduction

THE appearance of new services like high definition video streaming, mobility applications or cloud computing is increasing the demand of backbone bandwidth, saturating the current optical communication systems based on DWDM networks with 10–40 Gbps per carrier. To solve this problem the potential bandwidth of existing optical fiber networks has to be fully exploited. Modulations based on coherent detection and polarization multiplexing have been proposed to increase the transmission rate to 100–400 Gbps [1]. Receivers for this type of modulations comprise two parts: the polarization diversity network (polarization splitters or rotators), and the phase diversity network (90° hybrid and balanced photodiodes). Fig. 1 schematically shows a preferred implementation of this receiver. The polarization diversity network is composed of two polarization beam splitter (PBS) and the phase diversity and power detection network is composed by two single polarization coherent receivers (SPR). The aim of the PBS is feeding each SPR with the desired polarization, maximizing the rejection to the undesired polarization [2]. Due to the stringent fabrication tolerances of the integrated PBS, polarization diversity network is usually implemented in free-space optics, whereas SPR can be implemented in a single integrated planar lightwave circuit (PLC). Because of size and cost it would be desirable to integrate the PBSs and the single polarization receivers on the same PLC.

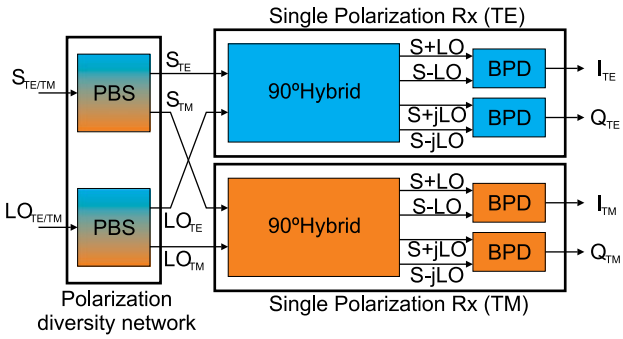

Fig. 1. Block diagram of a receiver for polarization multiplexed coherent optical communications.

Many approaches have been proposed to implement integrated PBS, based on: modal evolution [3], multimode interference couplers (MMI) [4], [5], directional couplers [6], and Mach–Zehnder interferometers (MZI) [7], [8]. MZI based PBS are of special interest due to its good performance, broad bandwidth and are usually the preferred option to integrate in an coherent receiver [9].

In this work a MZI based PBS compatible with a previously reported high performance InP coherent receiver [10], [11] is designed. We provide an in depth analysis on how thermal tuning of such a PBS can be used not only to compensate the effect of fabrication deviations, but also to achieve wavelength tunability. The PBS is monolithically integrated with a coherent receiver, and exhibits a polarization extinction ratio (PER) in excess of 16 dB tunable over the complete C-band. A peak extinction of 19 dB is achieved at $\lambda = 1545$ nm.

Manuscript received July 3, 2013; revised October 26, 2013; accepted November 25, 2013. Date of publication December 4, 2013; date of current version December 23, 2013. This work was supported in part by the Spanish Ministry of Science under Project TEC2009-10152 and in part by the European Mirthe Project FP7-2010-257980.

D. Pérez-Galacho, A. Ortega-Moñux, R. Halir, C. Alonso-Ramos, and Í. Molina-Fernández are with the Departamento de Ingeniería de Comunicaciones, ETSI Telecomunicación, Universidad de Málaga, 29010 Málaga, Spain (e-mail: diego.perez@ic.uma.es; aom@ic.uma.es; robert.halir@ic.uma.es; caar@ic.uma.es; imf@ic.uma.es).

R. Zhang, P. Runge, K. Janiak, G. Zhou, and H.-G. Bach are with the Fraunhofer Institute for Telecommunications, Heinrich-Hertz-Institute, Einsteinufer 37, D-10587 Berlin, Germany (e-mail: ruiyong.zhang@hhi.fraunhofer.de; patrick.runge@hhi.fraunhofer.de; klemens.janiak@hhi.fraunhofer.de; gan.zhou@hhi.fraunhofer.de; heinz-gunter.bach@hhi.fraunhofer.de).

A. G. Steffan is with with the u2t Photonics AG, Reuchlinstr, 10553 Berlin, Germany (e-mail: steffan@u2t.de).

Color versions of one or more of the figures in this paper are available online at http://ieeexplore.ieee.org.

Digital Object Identifier 10.1109/JLT.2013.2293782

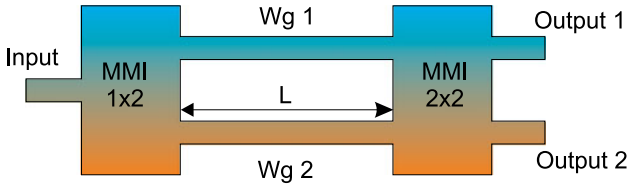

Fig. 2. Schematic of a generic MZI-PBS.

This paper is organized as follows. In Section II the design of the PBS is discussed. Section III is devoted to modeling the thermal tuning process to compensate fabrication errors. The performance of the receiver with the integrated PBS is presented in Section IV, focusing on the PER. Finally, Section V summarizes the main conclusions of this work.

II. PBS Design

The structure of a MZI based PBS is shown schematically in Fig. 2. It is composed of two MMI couplers interconnected by two waveguides, Wg_1 and Wg_2, of length L (arms of the interferometer). The MMI coupler at the input acts as a power divider whereas the MMI coupler at the output acts a 3 dB/90° coupler. The normalized power (P_1, P_2) at the two PBS outputs (output 1 and output 2 in Fig. 2) is given by [12]:

$$P_1^{\mathrm{TE/TM}} = 0.5\left[1+\sin\left(\left(\beta_2^{\mathrm{TE/TM}}-\beta_1^{\mathrm{TE/TM}}\right)L\right)\right]$$
$$P_2^{\mathrm{TE/TM}} = 0.5\left[1-\sin\left(\left(\beta_2^{\mathrm{TE/TM}}-\beta_1^{\mathrm{TE/TM}}\right)L\right)\right] \quad (1)$$

where β_1 and β_2 represent the propagation constants of the fundamental TE/TM modes of the waveguide arms. In case of perfect polarization splitting the power in each polarization is directed to different outputs, i.e. $P_1^{\mathrm{TE}}=1$, $P_1^{\mathrm{TM}}=0$, $P_2^{\mathrm{TE}}=0$ and $P_1^{\mathrm{TM}}=1$. As a figure of merit PER is defined as:

$$\mathrm{PER}_{\mathrm{TE}} = \frac{P_1^{\mathrm{TE}}}{P_1^{\mathrm{TM}}}$$
$$\mathrm{PER}_{\mathrm{TM}} = \frac{P_2^{\mathrm{TM}}}{P_2^{\mathrm{TE}}}. \quad (2)$$

In order to get perfect polarization splitting, the following two conditions should be fulfilled:

$$\left(\beta_2^{\mathrm{TE}}-\beta_1^{\mathrm{TE}}\right)L = \frac{\pi}{2}$$
$$\left(\beta_2^{\mathrm{TM}}-\beta_1^{\mathrm{TM}}\right)L = -\frac{\pi}{2} \quad (3)$$

solving for L in (3) the optimum interferometer arm length is found to be:

$$L = \frac{\pi}{\left(\beta_2^{\mathrm{TE}}-\beta_2^{\mathrm{TM}}\right)-\left(\beta_1^{\mathrm{TE}}-\beta_1^{\mathrm{TM}}\right)} = \frac{\pi}{\Delta\beta_2-\Delta\beta_1} \quad (4)$$

where $\Delta\beta_1$ and $\Delta\beta_1$ represent the modal birefringence of Wg_1 and Wg_2 respectively. Equation (4) clearly shows that the difference in modal birefringence in the arms of the interferometer should be maximized (i.e. $\Delta\beta_2 \gg \Delta\beta_1$) to minimize their lengths and thus maximizing the bandwidth of the PBS [12]. This can be done using waveguides with very dissimilar widths [7] or depositing a periodic layer stack on top of one of the waveguides [13].

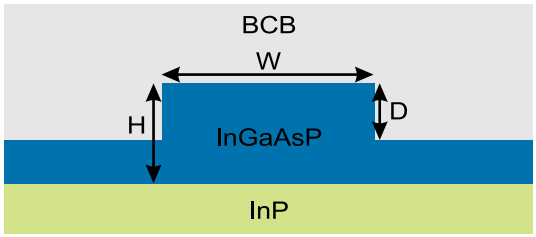

Fig. 3. Cross-section of the rib waveguide used in this work. The BCB cladding is removed on the waveguides with heaters.

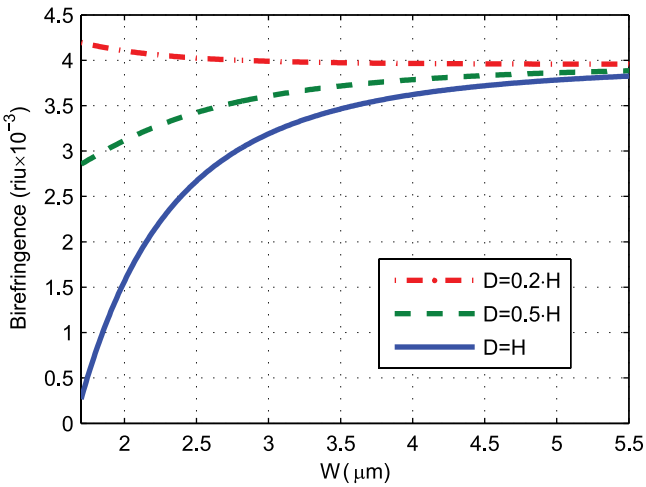

Fig. 4. Simulated birefringence of the rib waveguide used in this work as a function of the width for three different etch depths.

A. Design of Waveguide Cross-Section

To minimize complexity of fabrication process, we have chosen to maximize the difference in modal birefringence by engineering waveguide widths. Thus the waveguide used to implement the arms of the interferometer should provide a strong birefringence dependence on its width. The transversal geometry of the rib waveguide used to implement the arms of the interferometer is shown in Fig. 3, it is composed of a InGaAsP core over an InP substrate with an upper cladding of BCB. Waveguide modal birefringence ($\beta^{\mathrm{TE}}-\beta^{\mathrm{TM}}$) is studied as a function of its geometric parameters to find the optimum dimensions. The waveguide height ($H=1\,\mu$m) and the considered etch depths ($D=0.2H$, $0.5H$ and H) are fixed by compatibility considerations with our previously designed coherent receiver [10], [11], [14]. In Fig. 4 the modal birefringence of the waveguide is plotted as a function of width for these etch depths. It can be seen that the fully etched waveguide maximizes the differential modal birefringence achievable by changing the width, so the fully etched waveguide is the one chosen to design the PBS.

The adiabatic transition shown in Fig. 5 is used to convert the fully etched waveguides ($D=H$) in the PBS and the shallowly etched waveguides ($D=0.5H$) in the SPR. Simulated insertion losses better than 0.03 dB are provided for taper lengths ($\mathrm{L_{taper}}$) larger than 150 μm [10].

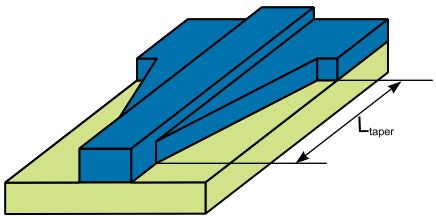

Fig. 5. Transition between two waveguides with different etch depth.

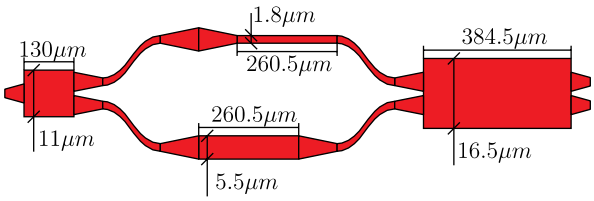

Fig. 6. Layout of the PBS with geometrical induced birefringence.

B. PBS With Geometrical Induced Birefringence

The design of the MZI based PBS comprises the design of a 1×2 MMI, a 2×2 MMI and the width and length of the MZI arms. The design and fabrication of MMI devices has been widely discussed in literature [15], [16], showing good performance and relaxed fabrication tolerances. The width and length of the MZI arms are designed using (3), (4) and the method proposed in [12]. The actual layout of the PBS is presented in Fig. 6. Adiabatic s-bends and tapers necessary to adapt the different waveguides cross-sections have been included. Note that a widening and narrowing taper has been included in the upper arm to cancel out phase shifts and losses induced by the tapers in the lower arm.

To evaluate the performance of the designed PBS, all structures were simulated using the 3-D full vectorial software FIMMWAVE varying the width of the MZI arms and the wavelength within the C-band (1530–1570 nm). Simulations show that PER is better than 20 dB in the whole C-band for the nominal design (without any width deviation). However small width deviations in the MZI arms have a significant impact on PER. The PER is reduced to 13 dB in C-band for a width deviation of ± 10 nm. However, width errors due to fabrication tolerances can be of the order of 100 nm. We thus propose to thermally tune the MZI arms to partially compensate fabrication errors.

III. Thermal Tuning

A heater is situated on top of each MZI arm and s-bends separate them so that each arm can be heated independently. To model the behavior of the thermal tuning, the effect of fabrication errors and the effect wavelength dispersion on the modal propagation constants are expressed as follows:

$$\beta_j^i = \beta_{0j}^i + S_{\beta_j}^{\lambda}\Big|_i \cdot \Delta\lambda + S_{\beta_j}^{W}\Big|_i \cdot \Delta W_j + S_{\beta_j}^{T}\Big|_i \cdot \Delta T_j \quad (5)$$

where $j = 1, 2$ refers to Wg_1 and Wg_2, $i =$ TE, TM refers to the polarization state and β_{0j}^i is the nominal propagation constant at the central wavelength (1550 nm). $\Delta\lambda$ and ΔW_j are the wavelength shift from the central wavelength and the width deviation from its designed value for Wg_j. Since the arms are close enough the width deviation will be the same for both arms (i.e. $\Delta W_1 = \Delta W_2 = \Delta W$). ΔT_j is the temperature increment of Wg_j with respect to the nominal operation temperature ($\Delta T_j = T_j - T_0$). $S_{\beta_j}^{\lambda}|_i$, $S_{\beta_j}^{W}|_i$ and $S_{\beta_j}^{T}|_i$ are the sensitivities of the propagation constant to changes in wavelength, width and temperature respectively. It is important to point out that sensitivities to wavelength and width depend on polarization and waveguide width. However, the sensitivity to temperature is virtually polarization and width independent, because: i) the heating process does not induce birefringence when considering the bulk materials ii) the thermo-optic coefficients for InP and InGaAsP have the same value ($2 \times 10^{-4} K^{-1}$). Thus, hereafter we consider $S_{\beta_j}^{T}|_i = S_{\beta}^{T}$.

TABLE I
Sensitivities to Temperature, Width and Wavelength for the Designed PBS

S_{β}^{T}	$S_{\Delta\beta}^{W}\big\vert_{\mathrm{TE}}$	$S_{\Delta\beta}^{W}\big\vert_{\mathrm{TM}}$	$S_{\Delta\beta}^{\lambda}\big\vert_{\mathrm{TE}}$	$S_{\Delta\beta}^{\lambda}\big\vert_{\mathrm{TM}}$
$1.2 \cdot 10^{-4}$	$-2.5 \cdot 10^{-2}$	$-2 \cdot 10^{-2}$	$3 \cdot 10^{-2}$	$2.9 \cdot 10^{-2}$
$(\mathrm{rad}/K{\cdot}\mu\mathrm{m})$	$(\mathrm{rad}/\mu\mathrm{m}^2)$	$(\mathrm{rad}/\mu\mathrm{m}^2)$	$(\mathrm{rad}/\mu\mathrm{m}^2)$	$(\mathrm{rad}/\mu\mathrm{m}^2)$

Recalculating $\mathrm{PER}_{\mathrm{TE/TM}}$ using (5), defining the differential propagation constant as $\Delta\beta = \beta_2 - \beta_1$ and operating (details are shown in the appendix), we obtain:

$$\begin{aligned} S_{\Delta\beta}^{\lambda}\big|_{\mathrm{TM}} \cdot \Delta\lambda_{\mathrm{TE}} &= -S_{\Delta\beta}^{W}\big|_{\mathrm{TM}} \cdot \Delta W - S_{\beta}^{T} \cdot \Delta T_{\mathrm{arms}} \\ S_{\Delta\beta}^{\lambda}\big|_{\mathrm{TE}} \cdot \Delta\lambda_{\mathrm{TM}} &= -S_{\Delta\beta}^{W}\big|_{\mathrm{TE}} \cdot \Delta W - S_{\beta}^{T} \cdot \Delta T_{\mathrm{arms}} \end{aligned} \quad (6)$$

where $S_{\Delta\beta}^{p}|_i$ is the sensitivity of the differential propagation constant to the parameter "p" for the polarization i, $\Delta\lambda_{\mathrm{TE}}$ and $\Delta\lambda_{\mathrm{TM}}$ are the shift of the wavelength response of $\mathrm{PER}_{\mathrm{TE}}$ and $\mathrm{PER}_{\mathrm{TM}}$ respectively. ΔT_{arms} is the difference between the temperatures of Wg_1 and Wg_2 ($\Delta T_{\mathrm{arms}} = T_2 - T_1$).

Paying attention to (6) it is observed that variations in the waveguide widths will shift the wavelength response of the PBS, unless they are compensated by thermal tuning. Sensitivities are calculated for the case of the designed PBS, the values are presented in Table I. Wavelength shifts are calculated using (6) and represented in Fig. 7, where wavelength shifts are plotted as a function of temperature difference for several width errors ($\Delta W = 0$, ± 50 and ± 75 nm). The mean wavelength shift is defined as $\overline{\Delta\lambda} = \frac{\Delta\lambda_{\mathrm{TE}} + \Delta\lambda_{\mathrm{TM}}}{2}$ and the differential wavelength shift $\Delta\lambda_{\mathrm{TE}} - \Delta\lambda_{\mathrm{TM}}$ in order to evaluate the impact on device performance. In Fig. 7 it can be seen that in the absence of width errors ($\Delta W = 0$) changes in the temperature difference tune the wavelength response of the device. Positive temperature differences ($\Delta T_{\mathrm{arms}} > 0$) yield blue shifts and negative temperature differences ($\Delta T_{\mathrm{arms}} < 0$) red shifts. When the device presents width errors ($\Delta W \neq 0$), the wavelength shift for TE differs from TM ($\Delta\lambda_{\mathrm{TE}} \neq \Delta\lambda_{\mathrm{TM}}$). The differential wavelength shift increases for greater width error. This differential wavelength shift cannot be cancelled by changing the temperature difference between the arms. Nevertheless, the temperature difference can be used to cancel the mean wavelength shift ($\overline{\Delta\lambda}$) or to tune the device to any operation wavelength within the C-band. For

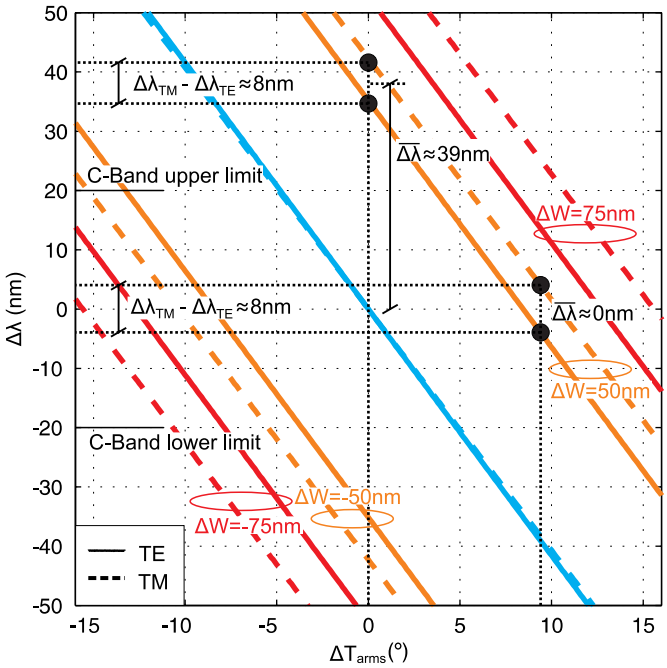

Fig. 7. Shift in the wavelength response as a function of the temperature difference between the MZI arms for several width errors (ΔW).

example: looking at the curves for $\Delta W = 50$ nm it can be seen that in absence of temperature difference ($\Delta T_{\text{arms}} = 0°$) the differential wavelength shift is 8 nm and the mean wavelength shift is $\overline{\Delta\lambda} = 39$ nm, shifting the response out of the C-band. The differential wavelength shift is small compared to the mean shift, because the difference between the sensitivities for TE and TM polarization states is small compared to their mean value [see Table I]. Setting the temperature difference to $\Delta T_{\text{arms}} = 9°$ the mean wavelength shift can be canceled. The response can also be tuned freely within the C-band changing the temperature difference between 5° and 13°.

The compensation process is qualitatively illustrated in Fig. 8, which represents PER as a function of wavelength for three different cases: i) nominal design, ii) device with errors, iii) compensated device. In the nominal design [see Fig. 8 (a)] the PER wavelength responses for TE and TM are both centered at the central wavelength. When the device is fabricated, introducing width errors [see Fig. 8 (b)], the PER wavelength responses are shifted away from the central wavelength and a differential wavelength shift between the TE and TM polarizations appears. Introducing a temperature difference between the MZI arms ($\Delta T_{\text{arms}} \neq 0$) the whole PER wavelength response can be shifted to the bandwidth of interest, but PER differential wavelength shift remains. This is illustrated in Fig. 8(c).

Thermal compensation is incorporated into the simulation of the PBS in order to evaluate the improvement in terms of width tolerances. $\text{PER}_{\text{TE/TM}}$ is calculated as a function of width error without using thermal compensation and introducing a temperature difference that, for each ΔW, optimizes PER at λ_0. The result is plotted in Fig. 9. It can be seen how in order to maintain PER over 20 dB at λ_0 without using thermal tuning ($\Delta T_{\text{arms}} = 0$) width errors should be lower than ± 10 nm,

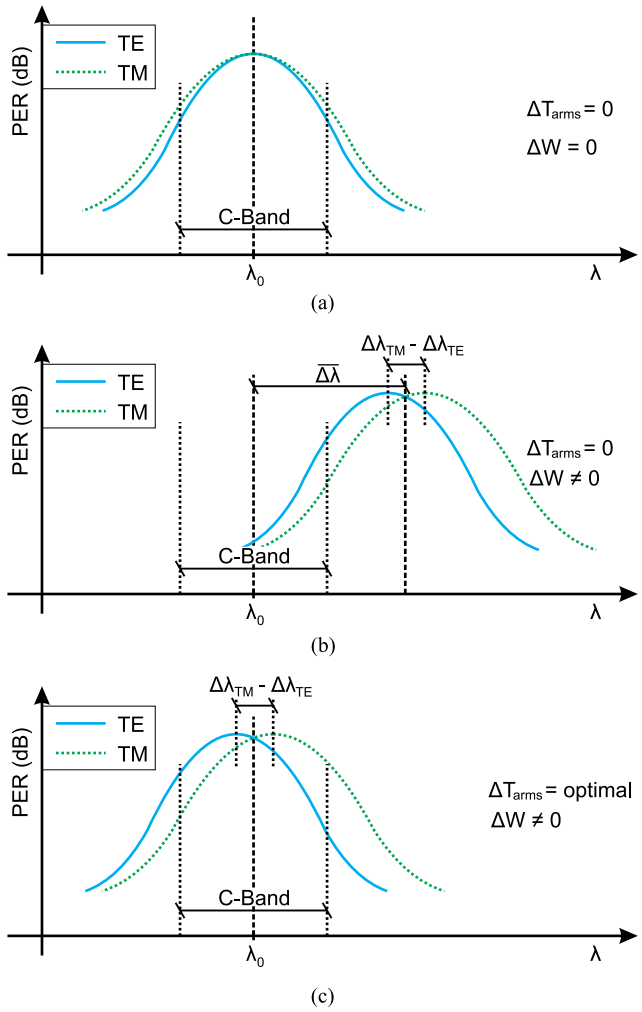

Fig. 8. Qualitative view of the thermal compensation process, PER as a function of wavelength for: (a) Nominal design, (b) device with errors, (c) compensated device.

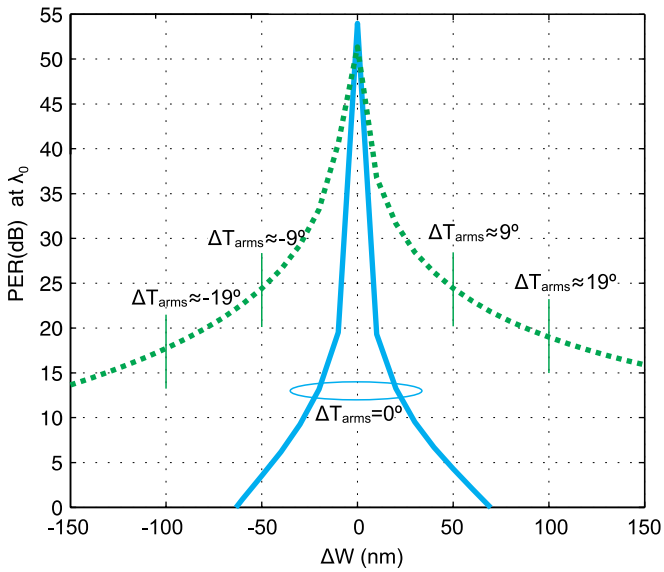

Fig. 9. PER at λ_0 as a function of width error for TE and TM polarization using thermal compensation and without thermal compensation (solid line, $\Delta T_{\text{arms}} = 0°$).

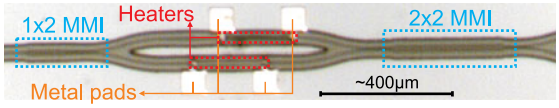

Fig. 10. Microscope image of one of the fabricated PBSs.

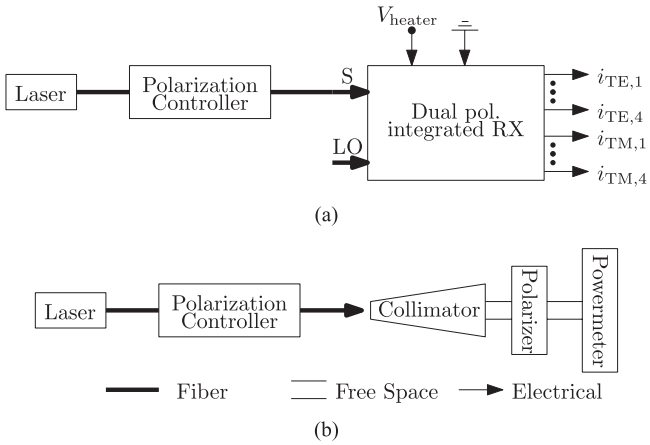

Fig. 11. (a) Measurement setup for PBS characterization, (b) setup for estimation of the maximum measurable PER.

whereas using thermal compensation width errors can be up to ±75 nm for a PER over 20 dB, which represents over a sevenfold improvement in terms of fabrication tolerances.

IV. Performance

The tunable PBS presented in the previous section has been monolithically integrated with a dual-polarization coherent receiver whose block diagram is schematically shown in Fig. 1. The receiver is fabricated on an InP/InGaAsP layerstack fully compatible with active-passive integration. The waveguides are RIE-etched using CH_4/H_2 into the guiding layer including an etch (descum) process to reduce scattering losses. Heaters are implemented with a metal layer stack of titanium, platinum and gold. In order to avoid thermal cross-talk between MZI arms, the cladding above the heaters is removed. The measured heater resistance (R_{heater}) is around 50 Ω. Light is coupled into the chip using integrated spot-size converters [17] while the output is done electrically, by means of waveguide integrated photodiodes [18]. The measurement setup is further detailed in the next section. Fig. 10 shows, for one of the fabricated receivers, a microscope image of a PBS. Metal pads are used to inject current into the waveguide heaters.

A. Description of the Measurement Setup

Fig. 11(a) shows a schematic representation of the measurement setup. Light from tunable laser passes through a polarization controller and is injected into the chip through one of the integrated spot-size converters. It then travels through the PBS and the 90° hybrids before reaching the output photodiodes [see Fig. 1]. For each polarization the photocurrent on the integrated photodiodes is recorded as the input wavelength is swept. Finally, the PER is computed from these measurements assuming that the polarization dependence of the 90° hybrids and the photodiodes is negligible. The temperature difference between the MZI arms (ΔT_{arms}) is controlled by means of the voltage applied to the corresponding heater pad (V_{heater}). Heater temperatures over the PBS were not been monitored during the experiments, so the tuning operation will be hereafter referred to as control voltage V_{heater}. The maximum PER that can be measured with our setup was determined using the scheme shown in Fig. 11(b), where the chip is substituted by a horizontally aligned polarizer and a powermeter. As the input polarization is varied with the polarization controller a maximum PER of around 25 dB is measured. The maximum PER measured with the chip is expected to be slightly lower, because precise alignment of the polarization with the chip axis is challenging, and minimum polarization conversion might take place within the chip.

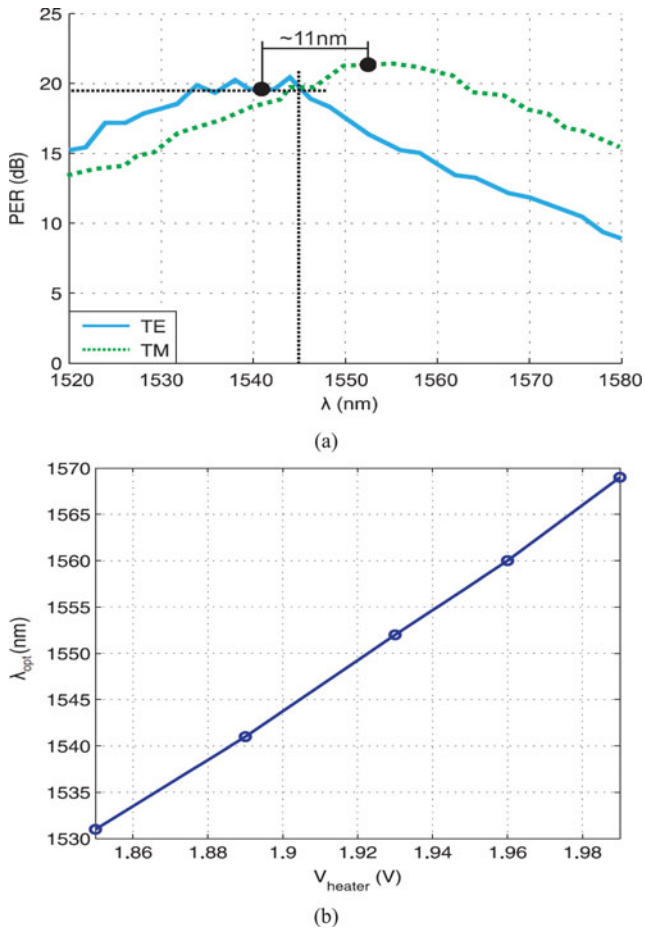

Fig. 12. (a) Measured as a function of wavelength, (b) wavelength at which PER is maximum as a function of heater voltage.

B. Measurements and Discussion

Results of PER measurements as a function of wavelength for one of the fabricated devices are shown in Fig. 12(a). A heater voltage of $V_{heater} \sim 1.92$ V was applied to obtain the highest possible PER over the complete C-band (1530–1570 nm). A maximum PER of 19 dB is obtained at $\lambda_{opt} = 1545$ nm, and a value above 12 dB is maintained over the complete C-band. The estimated insertion loss (IL) of the PBS is around

1.2 dB. Since the PBS is monolithically integrated within a dual-polarization coherent receiver, PBS losses cannot be measured directly. However, we have estimated this value measuring the IL of the whole chip and discounting the losses of the rest of the devices, which are well known from previous works [10], [11].

Although the width deviation of fabricated waveguides is not known, an estimation can be carried out using the model derived in the previous section and PER measurements shown in Fig. 12. The measured differential wavelength shift ($\Delta\lambda_{\mathrm{TE}} - \Delta\lambda_{\mathrm{TM}}$) is around 11 nm. This shift is consistent with a waveguide width deviation of 75 nm (see Fig. 7), which is within the margins of our fabrication process. The maximum PER predicted by the model for a fabrication error of 75 nm is around 20 dB (see Fig. 9), which is in good agreement with the measured PER at $\lambda_{\mathrm{opt}} = 1545$ nm. It must be pointed out that the derived model does not take into account the effects of the other circuitry in the chip (spot-size converters, 90° hybrids, interconnecting networks, coupling to photodiodes, etc.), so a perfect agreement between simulation and measurement cannot be expected.

One of the most important results of the theoretical model derived in the previous section is the wavelength tunability of the device. This means that heaters not only compensate fabrication errors but they also enable tuning of the PBS response to any wavelength within the C-band. Experimental validation of this idea is provided in Fig. 12(b), which shows the wavelength at which PER is maximum (λ_{opt}) as a function of the heater voltage ($\mathrm{V_{heater}}$). This curve has been obtained by measuring the PER within a wavelength range of 1520–1580 nm for different heater voltages, and then extracting the wavelength with maximum PER for both polarizations. From this figure it is clear that a nearly linear tuning of the wavelength response is obtained, which allows us to cover the complete C-band applying a heater voltage between 1.85 and 1.99 V. Heating power, calculated as $\mathrm{P_{heater}} = \mathrm{V^2_{heater}}/\mathrm{R_{heater}}$, is therefore around 80 mW. The measured PER at each λ_{opt} is always better than 16 dB.

V. Conclusion

The design and realization of an integrated MZI based PBS, fully compatible with a previously proposed coherent receiver [10], [11], has been presented. A theoretical model that explains how thermal tuning can simultaneously compensate fabrication errors and achieve wavelength tunability has been derived. Experimental results confirm the accuracy of the model. The fabricated PBS is tunable over the complete C-band with a PER in excess of 16 dB and insertion losses around 1.2 dB, for an estimated width fabrication error of ± 75 nm.

Appendix
Derivation of Equations (6)

PER is defined as:

$$\mathrm{PER_{TE}} = \frac{P_1^{\mathrm{TE}}}{P_1^{\mathrm{TM}}}$$
$$\mathrm{PER_{TM}} = \frac{P_2^{\mathrm{TM}}}{P_2^{\mathrm{TE}}}. \tag{A.1}$$

Introducing the expressions for $P_1^{\mathrm{TE/TM}}$ and $P_2^{\mathrm{TE/TM}}$ using (1) we obtain:

$$\mathrm{PER_{TE}} = \frac{1+\sin\left(\left(\beta_2^{\mathrm{TE}} - \beta_1^{\mathrm{TE}}\right)\cdot L\right)}{1+\sin\left(\left(\beta_2^{\mathrm{TM}} - \beta_1^{\mathrm{TM}}\right)\cdot L\right)}$$
$$\mathrm{PER_{TM}} = \frac{1-\sin\left(\left(\beta_2^{\mathrm{TM}} - \beta_1^{\mathrm{TM}}\right)\cdot L\right)}{1-\sin\left(\left(\beta_2^{\mathrm{TE}} - \beta_1^{\mathrm{TE}}\right)\cdot L\right)}. \tag{A.2}$$

Propagation constants are expressed as in (5):

$$\beta_j^i = \beta_{0j}^i + S_{\beta_j}^{\lambda}\Big|_i \cdot \Delta\lambda + S_{\beta_j}^{W}\Big|_i \cdot \Delta W_j + S_{\beta_j}^{T}\Big|_i \cdot \Delta T_j. \tag{A.3}$$

Nominal propagation constants are designed to fulfill:

$$\left(\beta_2^{\mathrm{TE}} - \beta_1^{\mathrm{TE}}\right)L = \frac{\pi}{2}$$
$$\left(\beta_2^{\mathrm{TM}} - \beta_1^{\mathrm{TM}}\right)L = -\frac{\pi}{2}. \tag{A.4}$$

Sensitivities to differential propagation constant are defined as:

$$S_{\Delta\beta}^{p}\big|_i = S_{\beta_2}^{p}\big|_i - S_{\beta_1}^{p}\big|_i. \tag{A.5}$$

Expressing propagation constants as in (A.3), introducing them in (A.2), using (A.4), (A.5) and operating the following is obtained:

$$\mathrm{PER_{TE}} = \frac{1+\sin\left(\frac{\pi}{2} + \varepsilon_{\mathrm{TE}}\cdot L\right)}{1+\sin\left(\frac{-\pi}{2} + \widehat{\varepsilon}_{\mathrm{TE}}\cdot L\right)}$$
$$\mathrm{PER_{TM}} = \frac{1-\sin\left(\frac{-\pi}{2} + \varepsilon_{\mathrm{TM}}\cdot L\right)}{1-\sin\left(\frac{\pi}{2} + \widehat{\varepsilon}_{\mathrm{TM}}\cdot L\right)} \tag{A.6}$$

where the errors $\varepsilon_{\mathrm{TE}}$, $\widehat{\varepsilon}_{\mathrm{TE}}$, $\varepsilon_{\mathrm{TM}}$ and $\widehat{\varepsilon}_{\mathrm{TM}}$ are given by:

$$\varepsilon_{\mathrm{TE}} = \Delta\lambda_{\mathrm{TE}}\cdot S_{\Delta\beta}^{\lambda}\Big|_{\mathrm{TE}} + \Delta W\cdot S_{\Delta\beta}^{W}\Big|_{\mathrm{TE}} + S_{\beta}^{T}\cdot\Delta T_{\mathrm{arms}}$$
$$\widehat{\varepsilon}_{\mathrm{TE}} = \Delta\lambda_{\mathrm{TE}}\cdot S_{\Delta\beta}^{\lambda}\Big|_{\mathrm{TM}} + \Delta W\cdot S_{\Delta\beta}^{W}\Big|_{\mathrm{TM}} + S_{\beta}^{T}\cdot\Delta T_{\mathrm{arms}}$$
$$\varepsilon_{\mathrm{TM}} = \Delta\lambda_{\mathrm{TM}}\cdot S_{\Delta\beta}^{\lambda}\Big|_{\mathrm{TM}} + \Delta W\cdot S_{\Delta\beta}^{W}\Big|_{\mathrm{TM}} + S_{\beta}^{T}\cdot\Delta T_{\mathrm{arms}}$$
$$\widehat{\varepsilon}_{\mathrm{TM}} = \Delta\lambda_{\mathrm{TM}}\cdot S_{\Delta\beta}^{\lambda}\Big|_{\mathrm{TE}} + \Delta W\cdot S_{\Delta\beta}^{W}\Big|_{\mathrm{TE}} + S_{\beta}^{T}\cdot\Delta T_{\mathrm{arms}}. \tag{A.7}$$

PER maximums occur when $\widehat{\varepsilon}_{\mathrm{TE}} = 0$ and $\widehat{\varepsilon}_{\mathrm{TM}} = 0$, the wavelength shifts ($\Delta\lambda_{\mathrm{TE}}$ and $\Delta\lambda_{\mathrm{TM}}$) that nullify them are the shifts of the PER wavelength response and are given by:

$$S_{\Delta\beta}^{\lambda}\big|_{\mathrm{TM}}\cdot\Delta\lambda_{\mathrm{TE}} = -S_{\Delta\beta}^{W}\big|_{\mathrm{TM}}\cdot\Delta W - S_{\beta}^{T}\cdot\Delta T_{\mathrm{arms}}$$
$$S_{\Delta\beta}^{\lambda}\big|_{\mathrm{TE}}\cdot\Delta\lambda_{\mathrm{TM}} = -S_{\Delta\beta}^{W}\big|_{\mathrm{TE}}\cdot\Delta W - S_{\beta}^{T}\cdot\Delta T_{\mathrm{arms}}. \tag{A.8}$$

References

[1] E. Ip, A. P. T. Lau, D. J. F. Barros, and J. M. Kahn, "Coherent detection in optical fiber systems," *Opt. Exp.*, vol. 16, no. 2, pp. 753–791, 2008.

[2] T. Barwicz, M. R. Watts, M. A. Popovic, P. T. Rakich, L. Socci, F. X. Kartner, E. P. Ippen, and H. I. Smith, "Polarization-transparent microphotonic devices in the strong confinement limit," *Nat. Photon.*, vol. 1, no. 1, pp. 57–60, 2007.

[3] W. Yuan, K. Kojima, B. Wang, T. Koike-Akino, K. Parsons, S. Nishikawa, and E. Yagyu, "Mode-evolution-based polarization rotator-splitter design via simple fabrication process," *Opt. Exp.*, vol. 20, no. 9, pp. 10163–10169, 2012.

[4] K. Kojima, W. Yuan, B. Wang, T. Koike-Akino, K. Parsons, S. Nishikawa, and E. Yagyu, "An mmi-based polarization splitter using patterned metal and tilted joint," *Opt. Exp.*, vol. 20, no. 26, pp. B371–B376, 2012.
[5] J. M. Hong, H. H. Ryu, S. R. Park, J. W. Jeong, S. G. Lee, E.-H. Lee, S.-G. Park, D. Woo, S. Kim, and B.-H. O, "Design and fabrication of a significantly shortened multimode interference coupler for polarization splitter application," *IEEE Photon. Technol. Lett.*, vol. 15, no. 1, pp. 72–74, Jan. 2003.
[6] L. M. Augustin, J. J. G. M. van der Tol, R. Hanfoug, W. J. M. de Laat, M. J. E. van de Moosdijk, P. W. L. van Dijk, Y.-S. Oei, and M. K. Smit, "A single etch-step fabrication-tolerant polarization splitter," *J. Lightw. Technol.*, vol. 25, no. 3, pp. 740–746, Mar. 2007.
[7] D. Dai, Z. Wang, J. Peters, and J. E. Bowers, "Compact polarization beam splitter using an asymmetrical Mach–Zehnder interferometer based on silicon-on-insulator waveguides," *IEEE Photon. Technol. Lett.*, vol. 24, no. 8, pp. 673–675, Apr. 2012.
[8] L. B. Soldano, A. I. de Vreede, M. K. Smit, B. H. Verbeek, E. G. Metaal, and F. H. Green, "Mach–Zehnder interferometer polarization splitter in ingaasp/inp," *IEEE Photon. Technol. Lett.*, vol. 6, no. 3, pp. 402–405, Mar. 1994.
[9] C. R. Doerr, L. Zhang, P. J. Winzer, N. Weimann, V. Houtsma, T. Hu, N. J. Sauer, L. L. Buhl, D. T. Neilson, S. Chandrasekhar, and Y. K. Chen, "Monolithic inp dual-polarization and dual-quadrature coherent receiver," *IEEE Photon. Technol. Lett.*, vol. 23, no. 11, pp. 694–696, Jun. 2011.
[10] R. Kunkel, H.-G. Bach, R. Zhang, D. Hoffmann, D. Schmidt, M. Schell, A. Ortega-Monux, S. Romero-Garcia, I. Molina-Fernandez, and R. Halir, "Design improvements for inp-based 90°-hybrid oeics for 100ge coherent frontends," in *Proc. Compound Semicond. Week, 23rd Int. Conf. Indium Phosphide Related Mater.*, 2011, pp. 1–4.
[11] P. Runge, S. Schubert, A. Seeger, K. Janiak, J. Stephan, D. Trommer, P. Domburg, and M. L. Nielsen, "Monolithic inp receiver chip with a 90° hybrid and 56 ghz balanced photodiodes," *Opt. Exp.*, vol. 20, no. 26, pp. B250–B255, 2012.
[12] D. Dai, Z. Wang, and J. E. Bowers, "Considerations for the design of asymmetrical Mach–Zehnder interferometers used as polarization beam splitters on a submicrometer silicon-on-insulator platform," *J. Lightw. Technol.*, vol. 29, no. 12, pp. 1808–1817, Jun. 2011.
[13] D. Pérez-Galacho, R. Halir, A. Ortega-Moñux, C. Alonso-Ramos, R. Zhang, P. Runge, K. Janiak, H.-G. Bach, A. G. Steffan, and I. Molina-Fernández, "Integrated polarization beam splitter with relaxed fabrication tolerances," *Opt. Exp.*, vol. 21, no. 12, pp. 14146–14151, 2013.
[14] C. Yao, H.-G. Bach, R. Zhang, G. Zhou, J. H. Choi, C. Jiang, and R. Kunkel, "An ultracompact multimode interference wavelength splitter employing asymmetrical multi-section structures," *Opt. Exp.*, vol. 20, no. 16, pp. 18248–18253, 2012.
[15] L. B. Soldano and E. C. M. Pennings, "Optical multi-mode interference devices based on self-imaging: Principles and applications," *J. Lightw. Technol.*, vol. 13, no. 4, pp. 615–627, Apr. 1995.
[16] R. Halir, I. Molina-Fernandez, A. Ortega-Monux, J. Wanguemert-Perez, D.-X. Xu, P. Cheben, and S. Janz, "A design procedure for high-performance, rib-waveguide-based multimode interference couplers in silicon-on-insulator," *J. Lightw. Technol.*, vol. 26, no. 16, pp. 2928–2936, Aug. 2008.
[17] C.-M. Weinert, "Design of fiber-matched uncladded rib waveguides on inp with polarization-independent mode matching loss of 1 db," *IEEE Photon. Technol. Lett.*, vol. 8, no. 8, pp. 1049–1051, Aug. 1996.
[18] H. G. Bach, A. Beling, G. Mekonnen, R. Kunkel, D. Schmidt, W. Ebert, A. Seeger, M. Stollberg, and W. Schlaak, "Inp-based waveguide-integrated photodetector with 100-ghz bandwidth," *J. Sel. Topics Quantum Electron.*, vol. 10, no. 4, pp. 668–672, Jul./Sep. 2004.

Diego Pérez-Galacho received the M.Sc. degree in telecommunication engineering from Málaga University, Spain, in 2011. Since 2011, he has been working on the design and development of photonic coherent receivers for the European project MIRTHE. His research currently focuses on devices based on subwavelength periodic structures and coherent receivers for optical communication with polarization diversity.

Ruiyong Zhang received the Dipl.-Ing. degree in electrical engineering from the Technical University-Berlin in 2009. Then he joined Fraunhofer Heinrich-Hertz-Institute (HHI) and worked as a Research Associate in the photodetector team. Since 2011, he has been the Project Leader of an EU founded project in HHI.

Alejandro Ortega-Moñux received the M.Sc. degree in telecommunications engineering in 1998 and the Ph.D. degree in 2008, both from the Málaga University, Spain. Since 1999, he has been with the ETSI Telecomunicacin, Universidad de Málaga, as an Assistant and then Associate Professor. His research interests include the area of the modeling and design of photonic integrated circuits, such as multimode interference couplers, fiber-chip grating couplers, polarization beam splitters and rotators or subwavelength periodic structures.

Robert Halir received the M.Sc. degree in telecommunications engineering (first-class Hons.) from Málaga University, Spain, in 2006. In the same year, he was awarded a FPU scholarship to carry out his thesis in silicon photonics. His work focused on the design and characterization of an integrated optical reflectometer, for which he received the Ph.D. degree from the Málaga University in 2010. He is currently an Assistant Professor at Málaga University, as well as a Researcher at the Andalusian Institute for Nano-medicine and Biotechnology (Bionand). His research interests include high performance silicon photonic devices, including ultra-broadband couplers, highly efficient fiber-to-chip couplers, and photonic biosensors.

Carlos Alonso-Ramos received the M.Sc. degree in telecommunications engineering from Málaga University, Spain, in 2008. Since 2009, he has been working toward the Ph.D. degree on integrated photonic circuits. Nowadays, he is working under a FPI scholarship supervised by Dr. A. Ortega. His main task is coupling diffraction gratings design. In collaboration with the National Research Council (NRC) in Canada, they have demonstrated efficient grating couplers in thick rib silicon-on-insulator waveguides for the first time. He also works on integrated polarization diversity management circuits. Together with the Heinrich Hertz Institute in Germany, they have developed a waveguide polarization rotator with simplified fabrication process. Together with the NRC and the Institut dElectronique Fondamentale in the University of Paris Sud in France, they have developed a new polarization rotation scheme with increased fabrication tolerances.

Patrick Runge was born in Berlin, Germany, in 1979. He received the Dipl.-Ing. degree in computer science and the Ph.D. degree in electrical engineering from the Technical University of Berlin, Germany, in 2005 and 2010, respectively. From 2005 to 2007, he was with Hymite GmbH, where he was involved in the RF design and measurement of optoelectronic packages for optical communication. In 2007, he returned to the Technische Universität Berlin to pursue the Ph.D. degree, where he investigated nonlinear effects and applications of ultralong semiconductor optical amplifiers. After finishing his Ph.D. degree, he worked from 2010 to 2011 for a patent attorney. Since 2011, has been with the Heinrich Hertz Institute where he is currently engaged in the development and fabrication of photodetectors based on InP.

Klemens Janiak received the Dipl.-Phys. degree in physics from the Technische Universitaet of Berlin in 1990. He joined Heinrich-Hertz-Institut (HHI) in 1991. He is FhG-HHIs Senior Expert on dry etching technology for the fabrication of components based on InP and has been responsible for process development and PIC/OEIC-fabrication in several national research and industrial projects. In this frame, he developed integrated optical field transformers for efficient and reliable fibre/chip butt-coupling. More recently, he was involved in research on photonic crystal structures as well as in developing optical board mountable laser-, SOA-, and photo diode array OEICs. He is currently the head of the Modulator Group within HHIs Photonic Components Department.

Gan Zhou studied electrical engineering at Shanghai Jiaotong University China and Technical University Berlin, where he received the M.Sc. and Dipl.-Ing degrees, respectively, in 2011. He is currently a Research Associate in photodetector team in Fraunhofer Heinrich-Hertz-Institute

Heinz-Gunter Bach was born in Dresden, Germany, on April 27, 1953. He received the M.S. degree in electrical engineering from Technical University (TU) of Berlin, Germany, in 1978. From 1978 to 1981, he was with the Hahn-Meitner-Institute Berlin, working on the electrical characterization of BCCDs. He received the Ph.D. degree from TU Berlin, Germany, in 1982. In 1981, he joined the Heinrich-Hertz-Institut für Nachrichtentechnik Berlin GmbH heading the electrical characterization group within the Photonics division. He was involved in III–V material characterization, heterostructure analysis, and device optimization. Furthermore, he was engaged in project management of topics like HEMT optimization, opto-electronic packaging and within the last 19 years on ultra-high-speed photodetector development and photoreceiver integration, like pinTWA and coherent receiver types for 100GE applications. He gives annual lectures at the Technical University on “optoelectronic semiconductor devices”, measurement techniques for semiconductor devices and supervises students and diploma works. He is the author and coauthor of more than 210 papers and contributions in five books. He is a Member of VDE, Elektrotechnischer Verein (ETV) e.V. / ITG and served as a Technical Committee Member of the International Conference on Optical Fiber Communications.

Andreas G. Steffan studied electrical engineering and physics at the RWTH Aachen, where he received the Dipl.-Ing. and Dipl.-Phys. degrees. In 2002, he received his Ph.D. degree from the University of Cambridge, U.K., and joined u2t Photonics AG, where he worked as a Project Manager on the development of transmitter, receivers, and test and measurement products, including modulators and pulsed laser sources. Since 2011, he has been the Head of the R&D Department at u2t, working on novel device concepts for advanced modulation formats.

Íñigo Molina-Fernández is a Full Professor and Leader of the photonics group at University of Málaga, Spain. He is the co-author of more than 70 international publications in microwave and photonic topics. He has been participating in more than 25 research and development national and international projects, being the leader of 12 of them